GEOPHYSICAL RESEARCH LETTERS, VOL. 25, NO.12, PAGES 2061-2064, JUNE 15, 1998

FAST satellite wave observations in the AKR source region

R. E. Ergun[1], C. W. Carlson[1], J. P. McFadden[1], F. S. Mozer[1], G. T. Delory[1], W. Peria[1], C. C. Chaston[1], M. Temerin[1], R. Elphic[2], R. Strangeway[3], R. Pfaff[4], C.A. Cattell[5], D. Klumpar[6], E. Shelly[6], W. Peterson[6], E. Moebius[7], and L. Kistler[7]

Abstract. The Fast Auroral SnapshoT (FAST) satellite has made observations in the Auroral Kilometric Radiation (AKR) source region with unprecedented frequency and time resolution. We confirm the AKR source is in a density depleted cavity and present examples in which cold electrons appeared to have been nearly evacuated ($n_{hot} > n_{cold}$). Electron distributions were depleted at low-energies and up-going ion beams were always present. Source region amplitudes were far greater than previously reported, reaching $2x10^{-4}$ $(V/m)^2/Hz$ (300 mV/m) in short bursts with bandwidths generally < 1 kHz. Intense emissions were often at the edge of the density cavity. Emissions were near or below the cold plasma electron cyclotron frequency in the source region, and were almost entirely electromagnetic. The $|E|/|B|$ ratio was constant as a function of frequency and rarely displayed any features that would identify a cold plasma cutoff or resonance.

Introduction

One of the outstanding features of the auroral zone are powerful radio emissions known as Auroral Kilometric Radiation [*Gurnett*, 1974]. Similar emissions have been observed from all of the magnetized planets [*Zarka*, 1992]. AKR propagates primarily in the *R-X* mode and is known to originate on auroral field lines in regions of depleted density where down-going, electrons are accelerated [*Benson and Calvert*, 1979, and references therein].

AKR is believed to be generated near the electron cyclotron frequency (f_{ce}) from the free energy of the non-Maxwellian auroral electron distribution. A loss cone instability amplified by a subtle relativistic effect was one of the first widely accepted growth mechanisms [*Wu and Lee*, 1979], later expanded into the "cyclotron maser instability". Viking observations suggest that AKR is generated by electron distributions with $df/dv_\perp > 0$ [*Louarn, et al.*, 1990]. These electron distributions had an absence of low-energy electrons and displayed a trapped electron population. Relativistic modifications were shown to be important in regions where the "hot" plasma density of the precipitating electrons dominates the plasma dispersion [*Pritchett*, 1984, *Pritchett and Strangeway*, 1985].

Viking satellite observations of the AKR source region [*Bahnsen et al.*, 1987; *de Feraudy et al.*, 1987; *Roux et al.*, 1993] showed intense emissions with a spectral peak within ~2.5% of the cold plasma electron cyclotron frequency (f_{ce}), occasionally extending below f_{ce}. The largest amplitudes were reported to be $\sim 10^{-6}$ $(V/m)^2/Hz$ (~50 mV/m).

[1]Space Sciences Laboratory, University of California, Berkeley, CA
[2]Los Alamos National Laboratory, Los Alamos, NM
[3]University of California, Los Angeles, CA
[4]Goddard Space Flight Center, Greenbelt, MD
[5]University of Minnesota, Minneapolis, MN
[6]Lockheed Martin, Palo Alto, CA
[7]University of New Hampshire, Durham

Paper number 98GL00570.
0094-8534/98/98GL-00570$05.00

In this article, we present electric and magnetic field observations in the AKR source region from the FAST satellite. The electron distributions are described in a companion paper [*Delory et al.*, 1998] and the instruments are described elsewhere [*Ergun et al.*, 1998; *Carlson et al.*, 1997]. FAST observations include the first digital waveform capture in the AKR source region. These data

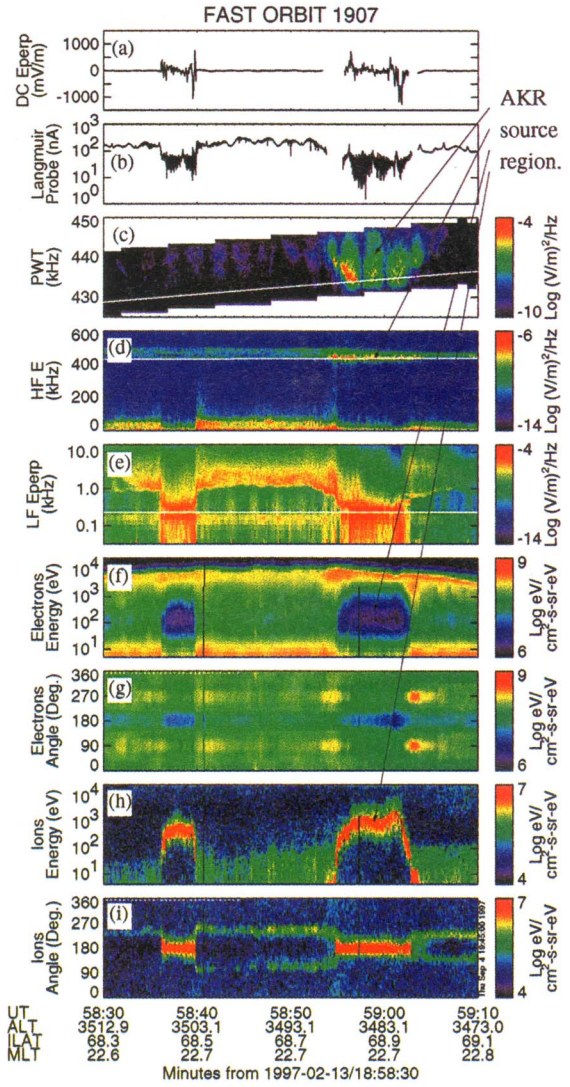

Figure 1. (a) The D.C. electric field. (b) Langmuir probe current. A 2 nA current roughly corresponds to ~1 cm^{-3} cold density or ~0.1 cm^{-3} hot density. (c) Wave power as measured by the Plasma Wave Tracker. The white line is f_{ce}. These data have spin modulations. The PWT covers a ~16 kHz band, the center frequency updated every 1 s. (d) High-frequency electric field power. The white line is f_{ce}. (e) Low-frequency, perpendicular wave power. The white line is f_{cH+}. (f-g) Electron energy flux versus energy and time and versus pitch angle and time. (h-i) Ion energy flux.

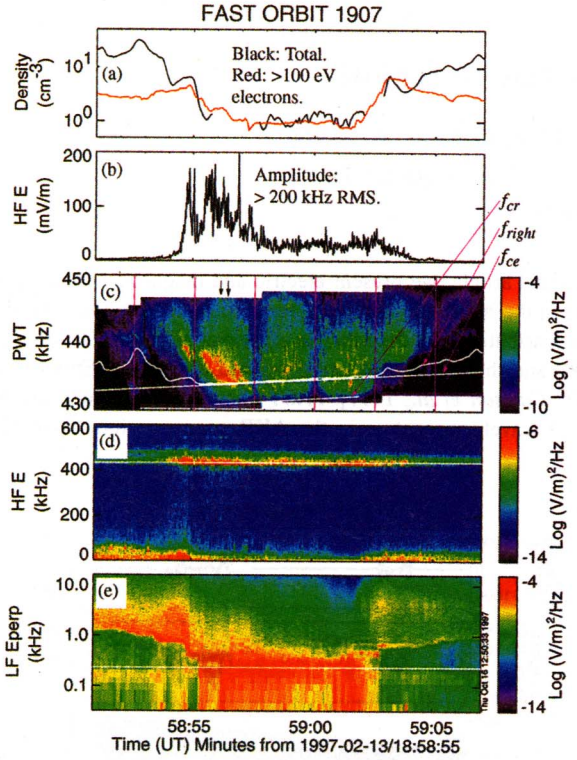

Figure 2. The AKR source region. (a) The total electron density (black) derived from fits to the whistler/Langmuir dispersion. The hot (>100 eV) electron density is in red. (b) The >200 kHz, RMS amplitude of $\boldsymbol{E}$. (c) Wave power as measured by the Plasma Wave Tracker. The white lines are f_{right}, f_{ce}, and f_{cr} ($eB/m\gamma$), with an uncertainty of ±400 Hz. The vertical lines mark when the antenna was nearly parallel to $\boldsymbol{B}_0$. (d) The high-frequency wave power. The white line is f_{ce}. (e) The perpendicular, low-frequency wave power. The white line is f_{cH+}.

have three axes of electric field ($\boldsymbol{E}$) and one axis of magnetic field ($\boldsymbol{B}$) at 0.5 μs resolution. We also present data from a relatively new instrument called a Plasma Wave Tracker, which measures the power within a ~16 kHz frequency band which includes f_{ce}. It has ~100 Hz frequency resolution and ~16 ms time resolution.

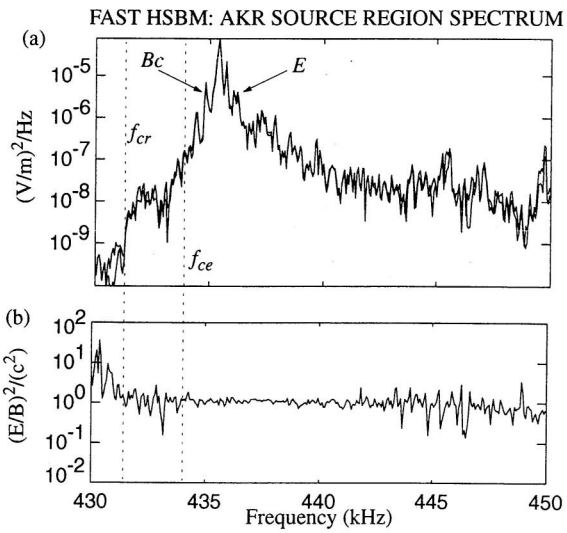

Figure 3. The AKR source region spectrum of $\boldsymbol{E}$ and $\boldsymbol{Bc}$ which were nearly identical and difficult to distinguish. The inter-calibration of $\boldsymbol{E}$ and $\boldsymbol{B}$ was made from free space emissions. The FWHM of the peak was less than 100 Hz.

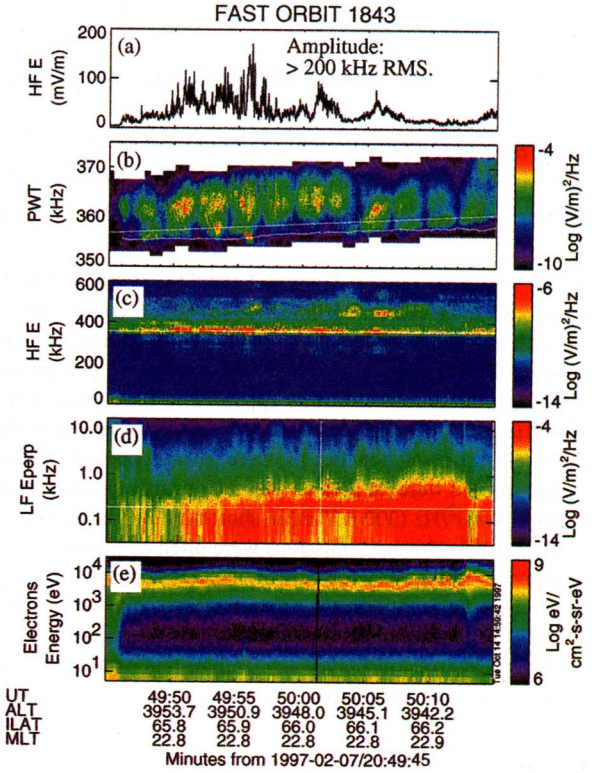

Figure 4. The AKR source region. (a) The >200 kHz, RMS amplitude of the $\boldsymbol{E}$. (b) Wave power as measured by the Plasma Wave Tracker. The white lines are f_{ce} (above) and f_{cr} (below) with an uncertainty of ±400 Hz. (c) The high-frequency electric field wave power. The white line is f_{ce}. (d) The perpendicular, low-frequency wave power. The white line is f_{H+}. (e) The electron energy flux versus energy. The fluxes at <60 eV were photoemissions.

Observations

Figure 1 shows high-resolution data covering ~40 s of a near-midnight auroral crossing at ~3500 km altitude. The display covers only a small portion of the auroral zone. Magnetometer data (not shown) indicate that the satellite was in the upward current region. We start by examining the D. C. electric field (panel a) and Langmuir probe current (panel b). There were two conspicuous periods, ~18:58:36 UT to ~18:58:40 UT and ~18:58:55 UT to ~18:59:02 UT, which had strong electric field turbulence and a noticeable decrease in the Langmuir probe current. The decrease in the Langmuir probe current signifies the auroral density cavity. The D.C. electric fields had electrostatic shocks which indicate that the satellite crossed a potential structure.

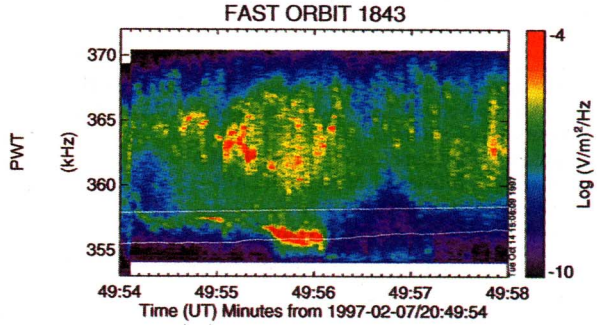

Figure 5. Plasma Wave Tracker observations show emissions near the relativistic electron cyclotron frequency (f_{cr}).

Panels f and g display electron energy flux versus energy and angle. There were ~1 keV to ~10 keV precipitating electrons throughout (panel f). In the two density cavities there were no electron fluxes below ~1 keV; fluxes below ~60 eV were spacecraft photoelectrons. The distribution was mostly isotropic (panel g) with reduced fluxes near 180° pitch angle (up-going) due to the ionospheric loss cone. There were, on several occasions, enhanced electron fluxes at 90° and 270° pitch angles. The most noticeable events were at ~18:58:54 UT and ~18:59:03 UT. The enhanced perpendicular electron fluxes had lower energies than the precipitating electrons and therefore were trapped [*Delory et al.*, 1998].

Up-going ion beams were seen in both density cavities. The ion energy in the first cavity was below 1 keV. In the second cavity it reached several kilovolts. Outside of the cavities, there were weak fluxes of transversely heated ions. The decreased density, electrostatic shocks, depleted low-energy electron fluxes, and ion beams were consistent with the spacecraft crossing into two regions that had parallel potential drops both above and below. Elsewhere, the spacecraft was below the auroral acceleration region.

Panels d and e show the electric field spectral power density as a function of frequency and time. Panel e displays the frequency span from 32 Hz to ~16 kHz at 32 Hz bandwidth and panel d displays D.C. to 600 kHz at 15 kHz bandwidth. The white lines are f_{ce} and the H+ cyclotron frequency (f_{cH+}). The data in panels d and e were derived from two antennae and are independent of the satellite's spin phase.

Panel c displays Plasma Wave Tracker (PWT) data. The frequency axis is from 425 kHz to 450 kHz with 64 Hz resolution. The PWT receives data from only one antenna so it is modulated by the satellite's spin. It has ~100 Hz jitter. The data show no enhancement of wave power in the first density cavity but do show strong AKR in the second density cavity that penetrated down to and below f_{ce}. The second density cavity, ~18:58:55 UT to ~18:59:02 UT, was an AKR source region. It was characterized by increased wave power near the f_{ce}, decreased plasma density, an absence of low-energy electrons fluxes, and an ion beam.

There were intense VLF emissions covering almost the entire 40 s period in Figure 1e. The emissions concentrated at or above the lower hybrid frequency (f_{lh} ~ 1 kHz) outside of the density cavities. f_{lh} abruptly decreased to near the f_{cH+} in the cavities.

Figure 2 shows an expanded view of the AKR source region. The black trace in panel a is the total electron density (n_{tot}) calculated from fits of $E_{\|}^2/E_{\perp}^2$ to the resonance cone angle of the whistler/Langmuir dispersion over the 1 kHz - 16 kHz frequency range [*Strangeway et al.*, 1998]. The fits used cold fluid dispersion with a thermal correction. We estimate an uncertainty of ~25% for densities greater than 4 cm^{-3}, and ~50% for densities of ~1 cm^{-3}. Fits with an RMS deviation greater than 50% were omitted. Strong thermal effects, electron acoustic emissions, or beam mode emissions could cause deviations in the fits.

The red trace in Figure 2a is the density of > 100 eV electrons measured by the electron electrostatic analyzer. This trace represents the "hot" electron density (n_{hot}) with an accuracy of ~20%. In this example, the electron density appears to have been primarily supported by energetic electrons, $n_{tot} \cong n_{hot}$. The data are consistent with no thermal core below ~100 eV.

Figure 2b displays the RMS amplitude of the > 200 kHz, omnidirectional electric field signal averaged over ~50 ms. The signal is dominated by AKR and has no satellite spin dependence and therefore represents the AKR amplitude "envelope". The AKR in this example reached amplitudes as high as 200 mV/m. The most intense emissions came in bursts of less than 1 s, during which the satellite traveled less than ~6 km.

Panels c, d, and e in Figure 2 are expanded views (15 s) of those in Figure 1. f_{ce} was calculated from the measured magnetic field with an uncertainty of ±0.1% (±400 Hz). Panel c, the PWT data, has several added features. The magenta lines indicate when the electric field antenna were nearly parallel to the magnetic field. The measured power was much lower at these times indicating the electric field signal was primarily perpendicular. The right cutoff, $f_{right} = (f_{ce} + (f_{ce}^2 + 4f_{pe}^2)^{1/2})/2$, where f_{pe} is the electron plasma frequency, was calculated from the total density in panel a and the measured magnetic field. The relativistic electron cyclotron frequency, $f_{cr} = eB/m\gamma$, corrects for the average energy of the >100 eV population in measured electron distribution. Since the bulk of the electron distribution was nearly mono-energetic, f_{cr} represents the electron cyclotron frequency of the hot electron population.

There are several interesting features in the AKR source region spectra. The emissions, at times, noticeably extended below f_{ce} (for example, 18:59:01.2 UT), but not below f_{cr}. Outside of the density cavity, the emissions seemed to obey the right cutoff. The AKR at ~18:58:54.75 UT and ~18:58:55.75 UT was at the boundary of the cavity. This particular event is strikingly similar to that reported on the Viking satellite [*Pottelette et al.*, 1992]. The density gradient had discrete steps and the most intense AKR was before the density reached its lowest value.

Figure 3a shows electric and magnetic field spectra superimposed. The spectra were calculated from part of a ~0.25 s digital waveform capture starting at ~18:58:56.18 UT (marked on Figure 2c). The $\boldsymbol{E}$ and $\boldsymbol{B}$ spectra were remarkably identical and difficult to distinguish. The FWHM bandwidth of the peak was quite narrow (~100 Hz). The $|\boldsymbol{E}|/|\boldsymbol{B}|$ ratio (Figure 3b) showed no feature that would identify f_{ce}, the upper hybrid resonance, or f_{right}. There was, however, a sharp reduction in wave power below f_{cr}.

During the digital capture (18:58:56.317 UT), one set of antennae was nearly parallel (1.3°) to the ambient magnetic field ($\boldsymbol{B}_0$). At that time, the AKR was peaking at > 300 mV/m. The ratio $\boldsymbol{E}_{\|}/\boldsymbol{E}_{\perp}$ was 0.040 indicating $\boldsymbol{E}$ was within 2.3° of perpendicular to $\boldsymbol{B}_0$. The average $\boldsymbol{E}_{\|}/\boldsymbol{E}_{\perp}$ from point by point de-spinning of the 3-axes digital data over the ~0.25 s capture was 0.063 (3.6°). Within error, the wave polarization is consistent with $k_{\|}=0$.

An AKR source region crossing during a second orbit is displayed in Figure 4 which plots 40 s of the near-midnight auroral zone. After 20:49:46 UT, the electric field emissions near f_{ce} intensify (panels a, b, and c) and there were no measurable electron fluxes below ~1 keV (panel e). The total plasma density, calculated from the low-frequency wave emissions, again was consistent with the hot (> 100 eV) plasma density measured by the electrostatic analyzers. The amplitude envelope (panel a) again showed intense bursts reaching almost 200 mV/m that often lasted less than one second. The majority of the AKR emissions (panel b) were 5 kHz to 10 kHz above f_{ce}, but the most intense burst (~20:49:56 UT) had a spectral peak measurably below f_{ce} and within error, at f_{cr}. Figure 5 shows an expanded view of panel b during the intense burst.

Discussion and Conclusions

Over one hundred orbits were inspected for AKR and more than ten AKR source regions have been examined. We confirm that the most intense AKR occurs in density depleted cavities extending 30 km to 300 km in latitude. All of the source regions were near magnetic midnight and close to the apogee of FAST (4175 km).

Observations from the FAST satellite have detailed the AKR source region with orders of magnitude higher time and frequency resolution than previous missions. As a result, the source region spectra are fully resolved and several new features of the AKR source region have emerged. Electron distributions had precipitat-

ing, energetic electrons with a loss cone and up-going ion beams were always present. The most outstanding features were a void of low-energy (<~1 keV) electron fluxes and an enhanced trapped population. High-resolution data show that the trapped electrons were near the edge of the density cavity rather than inside, clarifying previous reports [*Roux et al.*, 1993].

Detailed examinations revealed four examples of source region densities (~1 cm^{-3}) that were dominated by > 100 eV electrons, consistent with $n_{hot} > n_{cold}$ (the total density was not determined in the other orbits). How often this occurs is under investigation [*Strangeway et al.*, 1998]. FAST observations thus far indicate $f_{pe}/f_{ce} < 0.05$, which is less than previously reported [*Hilgers*, 1992].

Strong temporal and/or spatial variations were in every source crossing that was examined. The strongest emissions were often confined to the edge or to a small region in the density cavity and typically appeared in bursts < 1 s. The source region did not extend over the entire density cavity. The AKR source had an average spectral power density roughly one order of magnitude higher, and peak power typically two to three orders of magnitude higher than reported by Viking [*de Feraudy et al.*, 1987]. Peak electric field amplitudes were often greater than 100 mV/m and reached 300 mV/m. Source region amplitudes were such that the ratio of electric field energies to thermal energies ($W = \varepsilon_0 E^2/2n_e T_e$) were as high as 2.5×10^{-3} which may enable nonlinear wave-wave interactions. The source emissions had bandwidths often < 1 kHz and occasionally ~100 Hz. Outside of the source region, the FAST observations have comparable amplitudes to those reported earlier and remote, longer time-scale observations show similar rising and falling tones.

The most intense source region emissions were within ~2% of f_{ce} and occasionally below f_{ce}, but almost always above f_{cr}. Outside of the density cavity, a clear *R-X* cutoff was seen. The $|E|/|B|$ ratio showed that the source region emissions were electromagnetic, remarkably featureless, and revealed no indication of f_{ce}, f_{right}, nor the upper hybrid resonance. Only rarely was a possible electrostatic component observed. In one example, the wave polarization was shown to be < 3.6° from perpendicular to $\boldsymbol{B}_0$ and, within error, consistent with $k_{||} = 0$. This examples extends an earlier analysis which found the source polarization within 10° of $\boldsymbol{B}_0$ [*Hilgers et al.*, 1992]. These findings, the strongly depleted ($n_{hot} > n_{cold}$) density cavity, the near-perpendicular polarization, the emissions extending below f_{ce} to f_{cr}, and the constant ratio $|E|/|B|$ are consistent with strong modification of the plasma dispersion from the cold wave approximation [*Pritchett and Strangeway*, 1985], and wave growth below f_{ce} with $k = 0$ [Delory et al., 1988].

Acknowledgments. The authors thank R. Pottelette, A. Roux, and P. Louarn for there extremely helpful discussions. We also express our deep appreciation to the entire FAST team of scientists, engineers, and technicians. This research was conducted under NASA grant NAG5-3596.

References

Bahnsen, A. B., et al., Auroral hiss and kilometric radiation measured from the Viking satellite, *Geophys. Res. Lett.*, 14, 471, 1987.

Benson, R. F. and W. Calvert, ISIS-1 observations at the source of auroral kilometric radiation, *Geophys. Res. Lett.*, 6, 479, 1979.

Carlson et al., Design and applications of imaging plasma instruments, in *Monog. Meas. Techn. Space Plasma*, edited by R, Pfaff, AGU, 1998.

Delory, G. T. et al., FAST observations of electron distributions within AKR source regions, in press, *Geophys. Res. Lett.*, 1998.

de Feraudy, H., et al., Viking observations of auroral kilometric radiation from the plasmasphere to night auroral oval source regions, *Geophys. Res. Lett.*, 14, 511, 1987.

Ergun, R. E., et al., The FAST satellite electric and magnetic field instrument, Submitted, *Rev. Sci. Inst.*, 1998.

Gurnett, D. A., The Earth as a radio source: terrestrial kilometric radiation, *J. Geophys. Res.*, 79, 4227, 1974.

Hilgers, A., H. de Feraudy, and D. Le Queau, Measurement of the direction of the auroral kilometric radiation electric field inside the sources with the Viking satellite, *J. Geophys. Res.*, 97, 8381, 1992.

Hilgers, A., The auroral radiating plasma cavities, *Geophys. Res. Lett.*, 19, 237, 1992.

Louarn, P., et al., Trapped electrons as a free energy source for the auroral kilometric radiation, *J. Geophys. Res.*, 95, 5983, 1990.

Pottelette, R., R. A. Treumann, and N. Dubouloz, Generation of auroral kilometric radiation in upper hybrid wave-lower hybrid soliton interaction, *J. Geophys. Res.*, 97, 12029, 1992.

Pritchett, P. L., Relativistic dispersion and the generation of auroral kilometric radiation, *Geophys. Res. Lett.*, 11, 143, 1984.

Pritchett, P. L. and R. J. Strangeway, A simulation study of kilometric radiation along an auroral field line, *J. Geophys. Res.*, 90, 9650, 1985.

Roux, A., et al., Auroral kilometric radiation sources: in situ and remote observations from Viking, *J. Geophys. Res.*, 98, 11657, 1993.

Strangeway, R. J. et al., FAST observations of the auroral density cavity, submitted, *Geophys. Res. Lett.*, 1997.

Wu, C. S., and L. C. Lee, A theory of the terrestrial kilometric radiation, *Astrophys. J.*, 230, 621, 1979.

Zarka, P., The auroral radio emissions from planetary magnetospheres: what do we know, what don't we know, what do we learn from them? *Adv. Space Res.* 12 (8), 99, 1992.

C. W. Carlson, C. C. Chaston, G. T. Delory, R. E. Ergun, J. P. McFadden, F. S. Mozer, W. Peria, M. Temerin, Space Sciences Laboratory, University of California, Berkeley, CA 94720. (e-mail: cwc; ccc; gdelory; ree; mcfadden; mozer; peria; temerin@ssl.berkeley.edu)

R. Elphic, Los Alamos National Laboratory, D438, Los Alamos, NM 87545. (e-mail: relphic@lanl.gov)

R. Strangeway, IGPP, University of California, Los Angeles, CA 90095. (e-mail: strange@igpp.ucla.edu)

R. Pfaff, NASA Goddard Space Flight Center, Code 696, Greenbelt, MD 20771. (e-mail: rob.pfaff@gsfc.nasa.gov)

C. A. Cattell, Tate Laboratory of Physics, University of Minnesota, Minneapolis, MN 55455. (e-mail: cattell@belka.spa.umn.edu)

D. Klumpar, E. Shelly, W. Peterson, Lockheed Palo Alto Research Lab., Palo Alto, CA 94304. (e-mail: klump@agena.space.lookheed.com)

E. Moebius, L. Kistler, Morse Hall, University of New Hampshire, Durham, NH 03824. (e-mail: moebius; kistler@rotor.sr.unh.edu)

(Received October 31, 1997; revised February 4, 1998; accepted February 9, 1998.)